of the experiments in (*26*–*29*), wherein polarization entanglement is generated via post selection (see supporting online text and Fig. 4C). The mapping is performed assuming that quantum mechanics is correct (*1*, *27*–*29*). At $\tau = 0$, the predicted CHSH Bell's parameter is $S = 2.68(2)$, a violation of the Bell's inequality $|S| \leq 2$. The predicted violation is not closer to the theoretical maximum $S_{max} = 2\sqrt{2} \approx 2.828$ (dashed line of Fig. 4C), largely due to backgrounds set by the two-photon generation rate.

The frequency bandwidths of the write and read photons are 1.1(2) MHz, making them ideal for interacting with narrowband systems such as atoms, molecules, and optical cavities. By separately heterodyning the write and read photons with laser light derived from the π-pump laser (measured linewidth of 50 kHz), we obtained the power spectral density of the photons from the Fourier transform of the measured second-order autocorrelation function (Fig. 4D). The photons are nearly Fourier-transform limited, as can be seen from the 2-MHz full width at half-maximum power spectrum (Fig. 4E) of the measured cross-correlation function $g_{wr}(\tau)$ taken at slightly different parameters.

These measurements show that pairs of nearly identical photons are generated at an approximate rate of 5×10^4 pairs/s into a single Gaussian transverse mode. The spectral brightness of 5×10^4 pairs/s per MHz^{-1} is $\sim 10^3$ times as bright as the best sources based on parametric downconversion with nonlinear crystals (*8*). The system can operate very near fundamental limits on recovery efficiency, photon bandwidth, and two-photon suppression for a conditional single-photon source. In addition, identical photon pairs are necessary for certain quantum information protocols such as quantum computation with linear optics (*3*). The identical photon pairs also have potential applications for sub-shotnoise spectroscopy of atomic ensembles.

References and Notes

1. A. Aspect, P. Grangier, G. Roger, *Phys. Rev. Lett.* **49**, 91 (1982).
2. L.-M. Duan, M. D. Lukin, J. I. Cirac, P. Zoller, *Nature* **414**, 413 (2001).
3. E. Knill, R. Laflamme, G. Milburn, *Nature* **409**, 46 (2001).
4. Q. A. Turchette, C. J. Hood, W. Lange, H. Mabuchi, H. J. Kimble, *Phys. Rev. Lett.* **75**, 4710 (1995).
5. D. F. Phillips, A. Fleischhauer, A. Mair, R. L. Walsworth, M. D. Lukin, *Phys. Rev. Lett.* **86**, 783 (2001).
6. A. André, L.-M. Duan, M. D. Lukin, *Phys. Rev. Lett.* **88**, 243602 (2002).
7. B. Julsgaard, A. Kozhekin, E. S. Polzik, *Nature* **413**, 400 (2001).
8. F. Konig, E. J. Mason, F. N. C. Wong, M. A. Albota, *Phys. Rev. A.* **71**, 033805 (2005).
9. A. T. Black, J. K. Thompson, V. Vuletić, *Phys. Rev. Lett.* **95**, 133601 (2005).
10. C. H. van der Wal *et al.*, *Science* **301**, 196 (2003).
11. M. D. Eisaman *et al.*, *Phys. Rev. Lett.* **93**, 233602 (2004).
12. A. Kuzmich *et al.*, *Nature* **423**, 731 (2003).
13. C. W. Chou, S. V. Polyakov, A. Kuzmich, H. J. Kimble, *Phys. Rev. Lett.* **92**, 213601 (2004).
14. S. V. Polyakov, C. W. Chou, D. Felinto, H. J. Kimble, *Phys. Rev. Lett.* **93**, 263601 (2004).
15. D. Matsukevich, A. Kuzmich, *Science* **306**, 663 (2004).
16. C. K. Hong, Z. Y. Ou, L. Mandel, *Phys. Rev. Lett.* **59**, 2044 (1987).
17. C. Santori, D. Fattal, J. Vuckovic, G. S. Solomon, Y. Yamamoto, *Nature* **419**, 594 (2002).
18. T. Legero, T. Wilk, M. Hennrich, G. Rempe, A. Kuhn, *Phys. Rev. Lett.* **93**, 070503 (2004).
19. T. Legero, T. Wilk, A. Kuhn, G. Rempe, *Appl. Phys. B* **77**, 797 (2003).
20. V. Balić, D. A. Braje, P. Kolchin, G. Y. Yin, S. E. Harris, *Phys. Rev. Lett.* **94**, 183601 (2005).
21. J. F. Clauser, *Phys. Rev. D* **9**, 853 (1974).
22. M. D. Eisaman *et al.*, *Nature* **438**, 837 (2005).
23. C. W. Chou *et al.*, *Nature* **438**, 828 (2005).
24. T. Chaneliere *et al.*, *Nature* **438**, 833 (2005).
25. D. N. Matsukevich *et al.*, *Phys. Rev. Lett.* **96**, 030405 (2006).
26. J. F. Clauser, M. A. Horne, A. Shimony, R. A. Holt, *Phys. Rev. Lett.* **23**, 880 (1969).
27. Y. H. Shih, C. O. Alley, *Phys. Rev. Lett.* **61**, 2921 (1988).
28. Z. Y. Ou, L. Mandel, *Phys. Rev. Lett.* **61**, 50 (1988).
29. D. Fattal *et al.*, *Phys. Rev. Lett.* **92**, 037903 (2004).

30. This work was supported in parts by grants from NSF, Defense Advanced Research Projects Agency, Army Research Office, and the Sloan Foundation. J.S. acknowledges a National Defense Science and Engineering Graduate Fellowship from the U.S. Department of Defense. H.L. acknowledges a Josephine de Karman Fellowship and a A*STAR (Singapore) Scholarship.

Supporting Online Material

www.sciencemag.org/cgi/content/full/313/5783/74/DC1
SOM Text
References

21 March 2006; accepted 1 June 2006
10.1126/science.1127676

Surface Crystallization in a Liquid AuSi Alloy

Oleg G. Shpyrko,[1,2*] Reinhard Streitel,[1] Venkatachalapathy S. K. Balagurusamy,[1] Alexei Y. Grigoriev,[1] Moshe Deutsch,[3] Benjamin M. Ocko,[4] Mati Meron,[5] Binhua Lin,[5] Peter S. Pershan[1]

X-ray measurements reveal a crystalline monolayer at the surface of the eutectic liquid $Au_{82}Si_{18}$, at temperatures above the alloy's melting point. Surface-induced atomic layering, the hallmark of liquid metals, is also found below the crystalline monolayer. The layering depth, however, is threefold greater than that of all liquid metals studied to date. The crystallinity of the surface monolayer is notable, considering that AuSi does not form stable bulk crystalline phases at any concentration and temperature and that no crystalline surface phase has been detected thus far in any pure liquid metal or nondilute alloy. These results are discussed in relation to recently suggested models of amorphous alloys.

Surface melting—the coexistence of a liquid surface layer with the bulk crystal at temperatures below the bulk melting point T_m—has been observed in a wide range of materials (*1*, *2*) and occurs because the entropy of molecules at the free surface is greater than that in the bulk because of the reduced number of their near neighbors. The opposite effect, surface freezing, where a crystalline surface layer coexists with its molten bulk, is much rarer. Surface freezing has been observed, however, in complex liquids composed of high-anisotropy molecules, such as molten unary or binary alkanes and their derivatives (*3*), and in liquid crystals (*4*). Theory assigns the occurrence of this effect to the highly anisotropic shape of the molecules and to their lengths being greater than the interfacial width (*5*).

Freezing of the surface-segregated component into a two-dimensional (2D) solid layer has also been reported recently in the very dilute binary metallic alloys $Ga_{99.948}Pb_{0.052}$ (*6*) and $Ga_{99.986}Tl_{0.014}$ (*7*). A different ordering effect, surface-induced layering consisting of stratified layers (Fig. 1) near the vapor interface (*8*, *9*), has been observed in all liquid metals and alloys studied to date. The decay of the layering order with depth is exponential and has a range equal to the bulk liquid correlation length (two to three atomic diameters). No surface-parallel ordering was found within these layers in any elemental liquid metal. Similar layering, along with epitaxially induced surface-parallel order, has also been observed in both metallic and nonmetallic liquids near solid/liquid interfaces (*10*–*12*).

We present evidence for surface crystallization and enhanced surface layering in the liquid $Au_{82}Si_{18}$ eutectic alloy of a type unlike that previously reported for any liquid metal or alloy. A surface monolayer that exhibits lateral long-range crystalline order was found above the eutectic temperature $T_e = 359°C$. Beneath this monolayer, seven to eight layers occur that are liquid in the lateral direction but well defined in the normal direction. The crystalline surface monolayer and the enhancement of the

[1]Department of Physics and Division of Engineering and Applied Sciences, Harvard University, Cambridge, MA 02138, USA. [2]Center for Nanoscale Materials, Argonne National Laboratory, Argonne, IL 60439, USA. [3]Department of Physics, Bar-Ilan University, Ramat-Gan 52900, Israel. [4]Condensed Matter Physics and Materials Science Department, Brookhaven National Laboratory, Upton, NY 11973, USA. [5]Center for Advanced Radiation Sources, University of Chicago, Chicago, IL 60637, USA.

*To whom correspondence should be addressed. E-mail: oshpyrko@anl.gov

surface-induced layering range beyond the two to three layers observed in all other liquid metals studied to date clearly have a common origin. The surface-frozen monolayer undergoes a first-order transition into a different surface phase 12°C above T_e.

These unusual surface structures probably result from the equally unusual bonding properties of metastable amorphous bulk AuSi. AuSi, the first metallic alloy found to exhibit a glassy solid phase (*13*), remains one of the most puzzling amorphous solids. Silicon-rich amorphous AuSi is a semiconductor, has a low packing density, and has a low atomic coordination number (4 to 5). Its main structural motif is a continuous random network of covalently bonded Si atoms. The Au-rich alloy, however, is a metallic glass, almost as dense as a face-centered cubic lattice; has a high atomic coordination number (8 to 9); and has a random hard-sphere packing (*14*). Such random packing in amorphous metals was recently shown to consist of interpenetrating clusters, the outer atoms of which are shared by adjacent clusters (*15*, *16*). Because Si has a lower surface tension than Au, the surface of the liquid AuSi alloy is Si-rich, so atomic packing and bonding at the surface might be expected to be more like that of the covalently bonded Si-rich alloys than the metallic Au-rich bulk.

The existence of a very deep eutectic (for $Au_{82}Si_{18}$) at $T_e \approx 359$°C, much below T_m = 1063°C of Au and T_m = 1412°C of Si (Fig. 2A, inset), arises from the bonding effects discussed above. Below T_e, AuSi phase-separates in thermodynamic equilibrium into crystalline Au and Si, with no mutual solid solubility and no stable crystalline intermetallic compounds, whereas metastable amorphous AuSi phases can be achieved by rapid quenching, sputtering, and other techniques (*14*).

X-ray reflectivity off a liquid surface, $R(q_z)$, is measured as a function of the grazing angle of incidence α. Here $q_z = (4\pi/\lambda)\sin\alpha$ is the surface-normal wave vector transfer and λ is the x-rays' wavelength. The ratio R/R_F, where R_F is the theoretical reflectivity off of an ideally flat and abrupt liquid-vapor interface, depends on the surface-normal electron density profile ρ(*z*). A layered interface produces a Bragg-like peak in $R(q_z)/R_F(q_z)$ because of the constructive interference of the rays reflected from the periodically ordered surface layers (*8*). The larger the number of layers, the higher is the layering peak. Figure 2A demonstrates that the AuSi layering peak at 370°C is at least one order of magnitude higher than for the standard layering profile observed in all elemental liquids measured to date (*17*). This result implies that there are more than the two to three layers found in all previously measured liquid metals.

Indeed, a theoretical model fit to the measured values of $R(q_z)/R_F(q_z)$ (Fig. 2A, red line) yields the ρ(*z*) curve shown in Fig. 2B. Although the finer details of this ρ(*z*) curve may not be unique, two features were independent of the model used: the 2.5-nm-thick layering range (seven to eight well-defined atomic layers) and the Si enrichment of the top layer, indicated by a ρ value less than that of ρ_{bulk}, which corresponds to ~70 atomic % Si. This value agrees well with the 67 atomic % calculated from the Gibbs adsorption rule for an ideal binary solution (*18*).

No variation was found in the measured $R(q_z)$ from T_e = 359°C up to 371°C. At 371°C, $R(q_z)/R_F(q_z)$ changed abruptly (Fig. 2A, curve with black squares). By monitoring $R(q_z)$ at a fixed q_z while varying the temperature (Fig. 2B, inset), we found the surface phase transition at 371°C to be reproducible and to exhibit no hysteresis (<0.1°C). The narrow width of 0.17°C suggests a first-order phase transition.

The surface-parallel structure was explored by grazing incidence x-ray diffraction (GIXD). X-rays impinging on the liquid AuSi surface well below the critical angle penetrated the surface only evanescently, to a depth of ~1.4 nm (*19*), and produced a diffraction pattern for only the top ~5 atomic surface layers. The GIXD pattern measured for 359°C ≤ *T* ≤ 371°C (Fig. 3) showed sharp diffraction peaks indicative of long-range lateral ordering. A broad peak, characteristic of a liquid, was also observed. The GIXD pattern was indexed in a 2D rectangu-

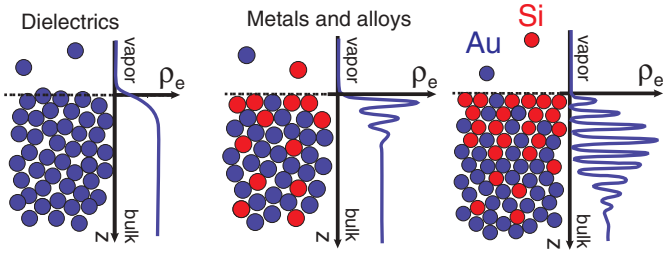

Fig. 1. Typical atomic surface structure and corresponding electron density profiles $\rho_e(z)$ of nonlayered dielectric liquids (**left**), standard layering in liquid metals and alloys (**middle**), and enhanced layering in AuSi (**right**).

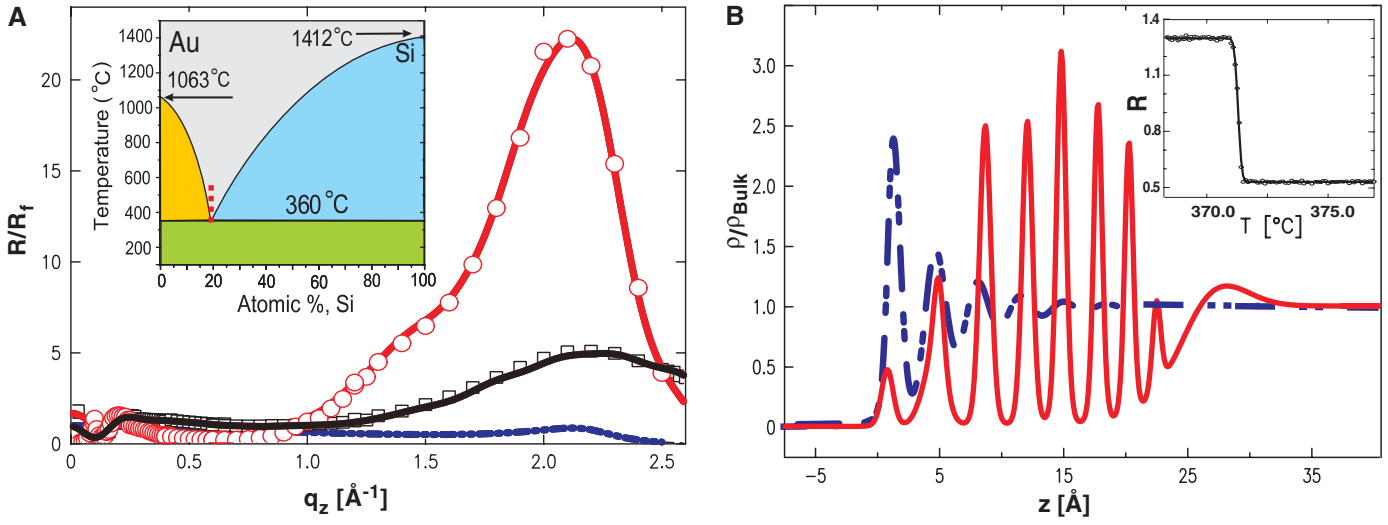

Fig. 2. (**A**) Fresnel-normalized x-ray reflectivity at 370°C (circles) and 375°C (squares), the corresponding model fits (red and black lines, respectively), and the curve expected for standard layering (dashed blue line). (Inset) Bulk phase diagram of AuSi. The gray area represents a liquid mixture phase, and the blue and yellow areas indicate the phase coexistence of solid Si or solid Au with a liquid alloy. The green area corresponds to phase-separated solid Au and solid Si. (**B**) Surface-normal electron density profiles corresponding to the same-line models in (A). (Inset) Reflectivity at fixed q_z = 1.0 Å^{-1} (circles) versus temperature, with a fit (black line) by an error function centered at 371.29°C with a width of 0.17°C.

lar lattice of dimensions a = 7.386 Å and b = 9.386 Å. A full-pattern refinement yielded the Au_4Si_8 structure shown in the right inset of Fig. 3. The high-T surface phase, which forms at 371°C and exists up to at least 410°C, also exhibits a set of sharp GIXD peaks but at different q_{xy} positions (*20*) than those of the 359°C < T < 371°C surface phase.

The GIXD peak intensities in the low-T phase were not affected by sample rotation around the surface-normal axis, indicating that the diffracting monolayer consists of a fine powder of randomly oriented crystallites. Debye-Scherrer analysis of the line shapes, measured with a high-resolution analyzer crystal, yields a typical crystallite size of ~ 2 to 10 μm. The measured Bragg rods (see the supporting online material) are surface-normal, indicating a quasi-2D crystalline structure. The ~1.5 $Å^{-1}$ width of the rod's q_z intensity distribution implies a crystalline layer thickness of d = $\pi/(1.5\ Å^{-1})$, where d is approximately equal to 2 Å (that is, a monolayer). This result agrees with the d value of ~2.5 Å that is estimated from the ratio of the integrated intensities of the GIXD peaks and the broad liquid peak.

Notably, despite the crystalline order, the capillary surface dynamics are still liquid-like; the diffuse scattering measured away from the specular peak exhibits a power-law behavior characteristic of the height-height correlations in liquid surfaces (*21*) (Fig. 3, left inset). The line shape of the diffuse scan (solid line in left inset of Fig. 3) is well reproduced by the capillary wave theory profiles if we use γ_{AuSi} = 780 mN/m convolved with the experimental resolution function. The agreement with capillary wave theory also indicates that in spite of the larger layering depth, the subsurface ordered layers are laterally liquid, as is the case for all previously measured liquid metals.

The crystalline AuSi monolayer's structure does not resemble those of pure Au, pure Si, or any of the reported metastable bulk intermetallics. However, crystalline phases with unit cell dimensions a = 7.44 Å and b = 9.33 Å, similar to those observed in our study, were reported in thin Au films deposited on a Si(111) surface (*22*). Some of these phases were thought to be surface phases, and some may exist also in the bulk. No reliable thicknesses of these phases could be obtained by the low-energy electron diffraction and Auger electron spectroscopy techniques that were used. A clear understanding of the formation mechanism, stability, and surface specificity of the crystalline phases in this system has not yet emerged (*23*). However, the strong Si-Si bonding (*24*) was suggested to play a crucial role, as well as the quasi-2D atomic coordination near the surface (*25*). In our case, the Gibbs adsorption surface enrichment by Si atoms is likely to facilitate the chemical Au-Si bonds that stabilize the crystalline surface layer but that evolve to metallic-like bonding away from the surface (*26*).

The Si packing in the crystalline surface monolayer (Fig. 3, right inset) resembles the covalently bonded, network-forming Si chains suggested to stabilize the amorphous structure of Si-rich AuSi alloys (*15*, *16*). A comparison of the unit cell structure presented in Fig. 3 with figure 1A of Miracle (*15*) indicates that the unit cell packing here is close to the interpenetrating cluster structure recently suggested as the main structural motif of bulk amorphous solids.

The formation of a surface-frozen phase is typically marked by a change in the slope of the surface tension versus temperature curve, $\gamma(T)$, from $d\gamma/dT > 0$ for a crystalline surface to $d\gamma/dT < 0$ for a liquid surface (*3*). Indeed, a positive slope is reported for AuSi above melting (*27*), in line with the crystalline phase reported here. The change to a negative slope, reported to occur at $T \approx$ 800° to 900°C (*27*), should indicate the melting of the ordered surface structure. Similar positive $\gamma(T)$ slopes above melting have been recently reported for AgSn, AgBi, AgIn, InCu, CuSn, MnSn, and AuZn binary alloys, implying that the formation of surface-frozen phases may not be an entirely uncommon phenomenon in multicomponent liquid alloys.

Beyond its importance for understanding the physics underlying amorphous metallic alloys, AuSi is also of high technological importance, because Au is widely used in interconnecting integrated circuits on Si substrates. AuSi also has important nanoscale applications such as the self-assembly of Si nanowires (*28*) and low-temperature bonding in micro- and nanoelectromechanical devices (*29*). Surface phases are of particular importance for nanotechnology, because properties of objects at the nanometer scale are expected to be dominated by surfaces and interfaces. The discovery of previously unidentified structures bridging the gap between 2D and 3D phases is expected, therefore, to have far-reaching consequences for both fundamental and applied research.

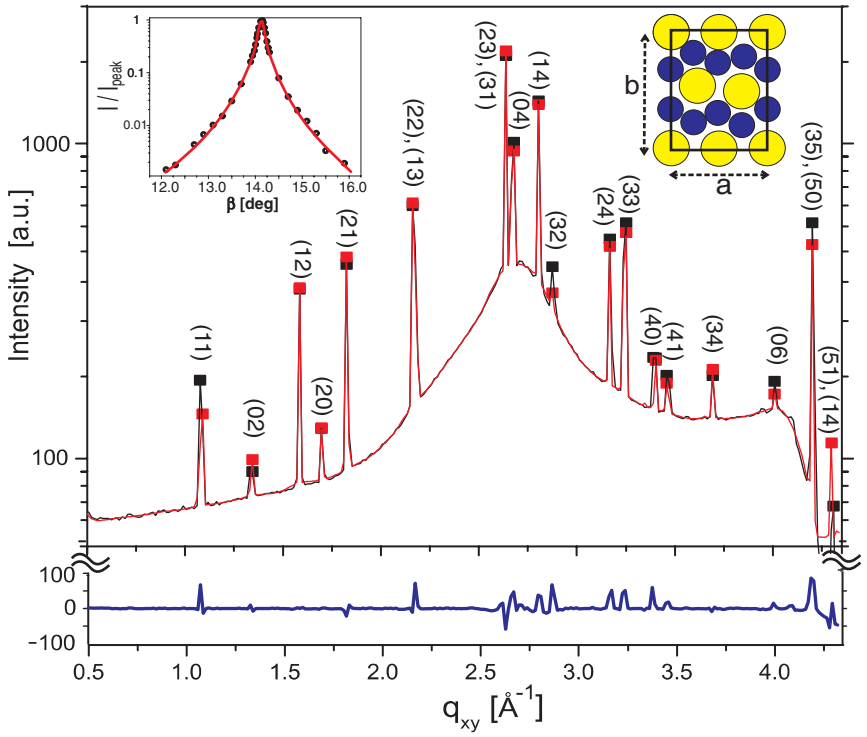

Fig. 3. Measured GIXD pattern (black line), theoretical fit (red line), and their difference (blue line) for the 359°C < T < 371°C surface phase. a.u., arbitrary units. (**Left inset**) Diffuse scattering profile versus the output detector angle β for a fixed incidence angle α = 14.11° and its fit (line) by the capillary wave theory prediction for γ = 780 mN/m. I/I_{peak} is the x-ray intensity normalized by the scan's peak intensity value. (**Right inset**) Crystal unit cell obtained from the GIXD pattern, where a = 7.386 Å and b = 9.386 Å. Au, yellow circles; Si, blue circles.

References and Notes

1. J. W. M. Frenken, J. F. Van der Veen, *Phys. Rev. Lett.* **54**, 134 (1985).
2. J. G. Dash, *Phys. Today* **38**, 26 (1985).
3. X. Z. Wu *et al.*, *Science* **261**, 1018 (1993).
4. Z. Dogic, *Phys. Rev. Lett.* **91**, 165701 (2003).
5. A. V. Tkachenko, Y. Rabin, *Phys. Rev. Lett.* **76**, 2527 (1996).
6. B. Yang, D. Gidalevitz, D. Li, Z.-q. Huang, S. A. Rice, *Proc. Natl. Acad. Sci. U.S.A.* **96**, 13009 (1999).
7. B. Yang, D. Li, S. A. Rice, *Phys. Rev. B* **67**, 212103 (2003).
8. O. M. Magnussen *et al.*, *Phys. Rev. Lett.* **74**, 4444 (1995).
9. M. J. Regan *et al.*, *Phys. Rev. Lett.* **75**, 2498 (1995).
10. S. E. Donnelly *et al.*, *Science* **296**, 507 (2002).
11. S. H. Oh, Y. Kauffmann, C. Scheu, W. D. Kaplan, M. Rühle, *Science* **310**, 661 (2005).
12. W. J. Huisman *et al.*, *Nature* **390**, 379 (1997).
13. W. Klement Jr., R. H. Willens, P. Duwez, *Nature* **187**, 869 (1960).

14. J. Weissmüller, *J. Non-Cryst. Solids* **142**, 70 (1992).
15. D. B. Miracle, *Nat. Mater.* **3**, 697 (2004).
16. H. W. Sheng *et al.*, *Nature* **439**, 419 (2006).
17. Our unpublished measurements on the liquid eutectic alloys of AuSn and AuGe yielded layering peaks 30 to 50 times lower than that of AuSi.
18. O. G. Shpyrko *et al.*, *Phys. Rev. Lett.* **95**, 106103 (2005).
19. Details of the GIXD experiment are available on *Science* Online.
20. Because of insufficient reproducibility, the discussion of this pattern must be deferred.
21. S. K. Sinha, E. B. Sirota, S. Garoff, H. B. Stanley, *Phys. Rev. B* **38**, 2297 (1988).
22. A. K. Green, E. Bauer, *J. Appl. Phys.* **47**, 1284 (1976).
23. J. F. Chang *et al.*, *Mat. Chem. Phys.* **83**, 199 (2004).
24. H. S. Chen, D. Turnbull, *J. Appl. Phys.* **38**, 3646 (1967).
25. S. L. Molodtsov, C. Laubschat, G. Kaindl, A. M. Shikin, V. K. Adamchuk, *Phys. Rev. B* **44**, 8850 (1991).
26. V. A. Filonenko, *Russ. J. Phys. Chem.* **43**, 874 (1969).
27. L. Bischoff, J. Teichert, T. Ganetsos, G. L. R. Mair, *J. Phys. D Appl. Phys.* **33**, 692 (2000).
28. J. B. Hannon, S. Kodambaka, F. M. Ross, R. M. Tromp, *Nature* **440**, 69 (2006).
29. Y. T. Cheng, L. W. Lin, K. Najafi, *J. Microelectromech. Syst.* **9**, 3 (2000).
30. This work was supported by the U.S. Department of Energy (DOE) grant DE-FG02-88-ER45379 and the U.S.-Israel Binational Science Foundation, Jerusalem. Brookhaven National Laboratory is supported by U.S. DOE contract DE-AC02-98CH10886. We acknowledge beamline assistance from J. Gebhardt, T. Graber, and H. Brewer at the Chemistry and Materials Science Sector of the Center for Advanced Radiation Sources (ChemMatCARS). ChemMatCARS Sector 15 is principally supported by NSF/DOE grant CHE0087817. The Advanced Photon Source is supported by U.S. DOE contract W-31-109-Eng-38.

Supporting Online Material

www.sciencemag.org/cgi/content/full/313/5783/77/DC1
Materials and Methods
Fig. S1
References and Notes

4 April 2006; accepted 25 May 2006
10.1126/science.1128314

Probing the Solvent-Assisted Nucleation Pathway in Chemical Self-Assembly

Pascal Jonkheijm,[1]* Paul van der Schoot,[2] Albertus P. H. J. Schenning,[1]† E. W. Meijer[1]†

Hierarchical self-assembly offers a powerful strategy for producing molecular nanostructures. Although widely used, the mechanistic details of self-assembly processes are poorly understood. We spectroscopically monitored a nucleation process in the self-assembly of π-conjugated molecules into helical supramolecular fibrillar structures. The data support a nucleation-growth pathway that gives rise to a remarkably high degree of cooperativity. Furthermore, we characterize a helical transition in the nucleating species before growth. The self-assembly process depends strongly on solvent structure, suggesting that an organized shell of solvent molecules plays an explicit role in rigidifying the aggregates and guiding them toward further assembly into bundles and/or gels.

Chemical self-assembly offers a very attractive approach for constructing complex, supramolecular nanostructures. Hierarchical processes, typical of chemical self-assembly, spontaneously produce ordered ensembles of single or multiple molecular components and are ubiquitous in chemistry, physics, materials science, and biology (*1*). For example, a large variety of molecules has been reported that form gels through three-dimensional networks of (bundles of) fibers (*2*). Highly versatile biomaterials have been produced by self-assembly of peptide amphiphiles (*3*), and (semi)conducting tubes and rods have been achieved from properly chosen π-conjugated oligomeric building blocks (*4*). In many cases, the resulting fibrillar structures are helical, and a preferred handedness is obtained by the introduction of stereocenters into the building blocks (*5*). Ensuring that the components aggregate in a specific motif, however, remains a formidable task; molecular components are easily trapped in kinetically stable arrangements of varying topology (*6*). The application of spectroscopy in combination with scattering and microscopy techniques has provided a reasonable view of the final self-assembled structures, yet a thorough understanding of the processes leading up to these structures remains elusive. Unravelling such structural pathways is crucial for the widely sought goal of extending rational synthesis into the nanoscale regime (*7*).

Although the growth of fibrillar structures typically requires nucleation, prior studies have not focused on the nature and properties of the nuclei. This lack of data is in sharp contrast to the abundant studies on the crystallization of small molecules (*8*) or polymers (*9*), and on the aggregation of proteins (*10*). For instance, notable insight into the formation of actin filaments, microtubules, and viral capsids by a nucleation-growth mechanism was obtained after the pioneering work of Klug (*11*) and Caspar (*12*). More recently, this insight was used to study pathologies stemming from amyloid deposits and diseases related to protein aggregation (*13*). Phenomenologically, the different phases of protein aggregation should be very similar to those involved in chemical self-assembly. Two models are commonly invoked to describe protein aggregation. Isodesmic self-assembly (*10*), also called multistage open association or ladder- or free-association model, is noncooperative, and the association constant is independent of the size of the object. Nucleated self-assembly, also called nucleation growth or initiation elongation, is characterized by a size-dependent association constant that gives rise to cooperative kinetics. We have sought to characterize such processes in chemical synthetic systems.

The fibrillar structures we examined comprise oligo(*p*-phenylenevinylene) derivatives (OPV-*x*) with chiral side chains capped on one end by a tridodecyloxybenzene and on the other by a ureidotriazine tailored for self-complementary fourfold hydrogen bonding (structure shown in Fig. 1) (*14*, *15*). Previous

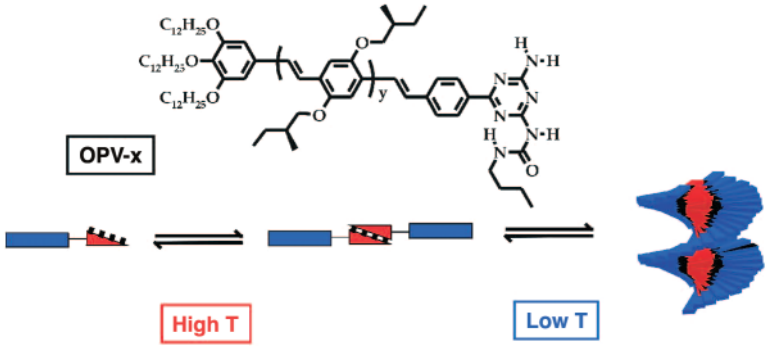

Fig. 1. Molecular structure of the oligo(*p*-phenylenevinylene) derivatives OPV-*x* [for OPV-3, *y* (number of dialkoxybenzene units) = 1; OPV-4, *y* = 2; and OPV-5, *y* = 3] and schematic representation of the self-assembly process, with blue blocks representing the OPV backbone and red wedges representing the hydrogen-bonding end groups.

[1]Laboratory of Macromolecular and Organic Chemistry, [2]Polymer Physics Group, Eindhoven University of Technology, Post Office Box 513, 5600 MB Eindhoven, Netherlands.

*Present address: Chemical Biology, Max Planck Institute for Molecular Physiology, Otto Hahnstrasse 11, 44227 Dortmund, Germany.

†To whom correspondence should be addressed. E-mail: e.w.meijer@tue.nl (E.W.M.); a.p.h.j.schenning@tue.nl (A.P.H.J.S.)